Available online at www.sciencedirect.com

SciVerse ScienceDirect

Ceramics International 39 (2013) 6343–6353

CERAMICS INTERNATIONAL

www.elsevier.com/locate/ceramint

Effects of manganese substitution at the B-site of lanthanum-rich strontium titanate anodes on fuel cell performance and catalytic activity

Manas K. Rath[a], Byung-Guk Ahn[a], Byung-Hyun Choi[b], Mi-Jung Ji[b], Ki-Tae Lee[a,c,*]

[a]Division of Advanced Materials Engineering, Chonbuk National University, Jeonbuk 561-756, Republic of Korea
[b]Optic and Electronic Ceramics Division, Korea Institute of Ceramic Engineering and Technology, Seoul 153-801, Republic of Korea
[c]Hydrogen and Fuel Cell Research Center, Chonbuk National University, Jeonbuk 561-756, Republic of Korea

Received 27 December 2012; received in revised form 18 January 2013; accepted 18 January 2013
Available online 24 January 2013

Abstract

$Sr_{0.4}La_{0.6}Ti_{1-x}Mn_xO_{3-\delta}$ with rhombohedral structure has been investigated in terms of their electrochemical performance, redox stability, and electro-catalytic properties for solid oxide fuel cell anodes. The performance of $Sr_{0.4}La_{0.6}Ti_{1-x}Mn_xO_{3-\delta}$ anodes for solid oxide fuel cells strongly depends on the Mn substitution at the B-site of the perovskites. Electrical conductivity of $Sr_{0.4}La_{0.6}Ti_{1-x}Mn_xO_{3-\delta}$ increases with increasing Mn content. X-ray photoelectron spectroscopy analysis reveals that the amount of Mn^{3+} and Ti^{3+}, which is an electronic charge carrier, increases with Mn doping. The reduced anode powders with high Mn/Ti ratio show oxygen storage capability and a low carbon deposition rate. Linear thermal expansion coefficients of $Sr_{0.4}La_{0.6}Ti_{1-x}Mn_xO_{3-\delta}$ anodes range from $9.46\times10^{-6}\,K^{-1}$ to $11.3\times10^{-6}\,K^{-1}$. The maximum power densities of the single cell with the $Sr_{0.4}La_{0.6}Ti_{0.2}Mn_{0.8}O_{3-\delta}$ anode in humidified H_2 and CH_4 at 800 °C are $0.29\ W\,cm^{-2}$ and $0.24\ W\,cm^{-2}$, respectively.

Keywords: C. Strontium titanate; E Solid oxide fuel cells; Carbon deposition; Oxide anodes

1. Introduction

Solid oxide fuel cells (SOFCs) are energy conversion devices that directly change chemical energy into electrical energy [1]. One of the major features of SOFCs is the high operating temperature, which allows the use of a variety of fuels and improves the conversion efficiency. Nickel–yttria stabilized zirconia (Ni–YSZ) is the state-of-the-art anode material. Although Ni shows excellent catalytic activity for the oxidation of hydrogen fuel, there are some disadvantages, such as low tolerance for sulfur, poor redox stability, and agglomeration after long-term operation. In particular, the carbon deposits derived from the hydrocarbon fuel result in performance degradation. From this perspective, current research on SOFCs is dedicated to develop advanced oxide-based anode materials which have high catalytic activity and tolerance for carbon deposition.

Various perovskite oxides such as chromates, titanates, and vanadates have been intensively investigated as alternative anode materials for hydrocarbon fuel use [2–6]. $SrTiO_3$ is an important class of electronic ceramics with an extensive range of electrochemical and electro-catalytic properties as well as good stability in both reducing and oxidizing atmospheres [7,8]. The donor-doped $SrTiO_3$ also shows interesting properties. Among various possible donor dopants, La^{3+} (1.36 Å) is a suitable candidate due to its similar ionic radius with Sr^{2+} (1.44 Å). It has been reported that La-doped $SrTiO_3$ shows n-type semiconducting behavior under reducing conditions. Further, the electrical conductivity in the La-doped $SrTiO_3$ increases with increasing concentration of La and/or decreasing $p(O_2)$ [7–9]. While the La-doped $SrTiO_3$ materials show dimensional and chemical stability under redox cycling, they have relatively poor electro-catalytic activity for H_2 oxidation in reducing atmospheres [8]. The transport properties and electro-catalytic activity of the La-doped

---

*Corresponding author at: Chonbuk Natioanl University, Division of Advanced Materials Engineering, 664-14 Deokjin-dong 1ga, Deokjin-gu, Jeonbuk 561-756, Republic of Korea. Tel.: +82 63 270 2290; fax: +82 63 270 2386.

E-mail address: ktlee71@jbnu.ac.kr (K.-T. Lee).

0272-8842/$ - see front matter © 2013 Elsevier Ltd and Techna Group S.r.l. All rights reserved.
http://dx.doi.org/10.1016/j.ceramint.2013.01.060

$SrTiO_3$ for fuel oxidation should be improved prior to use as an anode in hydrocarbon fuel SOFCs.

A suitable modification for the La-doped $SrTiO_3$ anodes can be achieved by substituting an appropriate dopant at the Ti site. For instance, the redox stability and conductivity of $La_{0.67}Sr_{0.33}Ti_{0.92}\times_{0.08}O_{3+\delta}$ with X=Ti, Al, Fe, Mg, and Sc is strongly affected by the choice of the dopant [10]. Tao et al. proposed Mn-doped $(La,Sr)CrO_3$ ($La_{0.75}Sr_{0.25}Cr_{0.5}Mn_{0.5}O_{3-\delta}$) as an effective anode, which showed high performance with low polarization loss in both humidified H_2 and CH_4 [11]. This high performance could be due to the presence of Mn^{3+} in the Cr^{4+} sites, which enhances the conductivity of the $La_{0.75}Sr_{0.25}Cr_{0.5}Mn_{0.5}O_{3-\delta}$ anode by generating oxygen vacancies in reducing atmospheres and high temperatures. Oxygen vacancies in the lattice may facilitate oxygen ion migration, which makes $La_{0.75}Sr_{0.25}Cr_{0.5}Mn_{0.5}O_{3-\delta}$ a mixed ionic–electronic conductor (MIEC). This incorporation and formation of the oxygen vacancy in $La_{0.75}Sr_{0.25}Cr_{0.5}Mn_{0.5}O_{3-\delta}$ under redox cycling is possible due to the multi-valance of Mn (+2, +3, and +4) doped at the B-site [2]. Meanwhile, it has also been reported that the partial replacement of Ti with Mn in $La_{4+x}Sr_{8-x}Ti_{12}O_{38-\delta}$ considerably improved the electrochemical performance [12]. The Mn-doped $La_{4+x}Sr_{8-x}Ti_{12}O_{38-\delta}$ shows mixed ionic–electronic conduction behavior, which extends the three-phase boundary onto the anode surface, resulting in considerable catalytic enhancement [12].

In this work, we formulate a new series of redox stable anodes with a wide range of Mn substitution for the Ti site in $Sr_{0.4}La_{0.6}TiO_3$ to improve the electrochemical performance in H_2 and CH_4 fuels. The La-rich composition is expected to allow a wide range of Mn substitution and valance defect structures. The effects of Mn content on the electrical conductivity, thermal expansion, defect structure, chemical compatibility, and electrochemical performance are presented.

2. Experimental procedures

2.1. Powder synthesis

$Sr_{0.4}La_{0.6}Ti_{1-x}Mn_xO_{3-\delta}$ (x=0.2, 0.4, 0.6 and 0.8) were synthesized by a combustion method using sucrose and pectin as the fuel and catalyst for combustion, respectively. The raw materials used in this study were $La(NO_3)_3\cdot xH_2O$ (Aldrich, 99.9% metal basis), $Sr(NO_3)_2$ (Alfa Aesar, 99.0%), $Mn(NO_3)_2\cdot 4H_2O$ (Alfa Aesar, 98%), titanium (IV) isopropoxide (Aldrich, 97%), 2-methoxyethanol (Alfa Aesar, 99%), sucrose (Alfa Aesar, 99%), and pectin (Aldrich). The flowchart for the combustion method is described in Fig. 1.

The composite cathode powder of $Ba_{0.6}Sr_{0.4}Co_{0.5}Fe_{0.5}O_{3-\delta}$–$Ce_{0.8}Gd_{0.2}O_{2-\delta}$ (BSCF–GDC) was also prepared using a combustion method. Raw materials used for powder processing were $Ba(NO_3)_2$ (Alfa Aesar, 99%), $Sr(NO_3)_2$ (Alfa Aesar, 99.0%), $Co(NO_3)_3\cdot 6H_2O$ (Aldrich, 98%+ ACS), $Fe(NO_3)_3\cdot 9H_2O$ (Alfa Aesar, 98~%, Alfa Aesar), $Ce(NO_3)_3\cdot 6H_2O$ (Aldrich, 99% metal basis), and $Gd(NO_3)_3\cdot xH_2O$ ($x\sim 6$, Alfa Aesar, 99.9%, REO). The powder processing techniques used were similar to those for the anode materials.

2.2. Material characterization

The synthesized anodes were characterized by X-ray diffraction (XRD) using Cu-K_α radiation for phase analysis. Morphology and elemental analysis for the synthesized powders were evaluated by scanning electron microscopy/

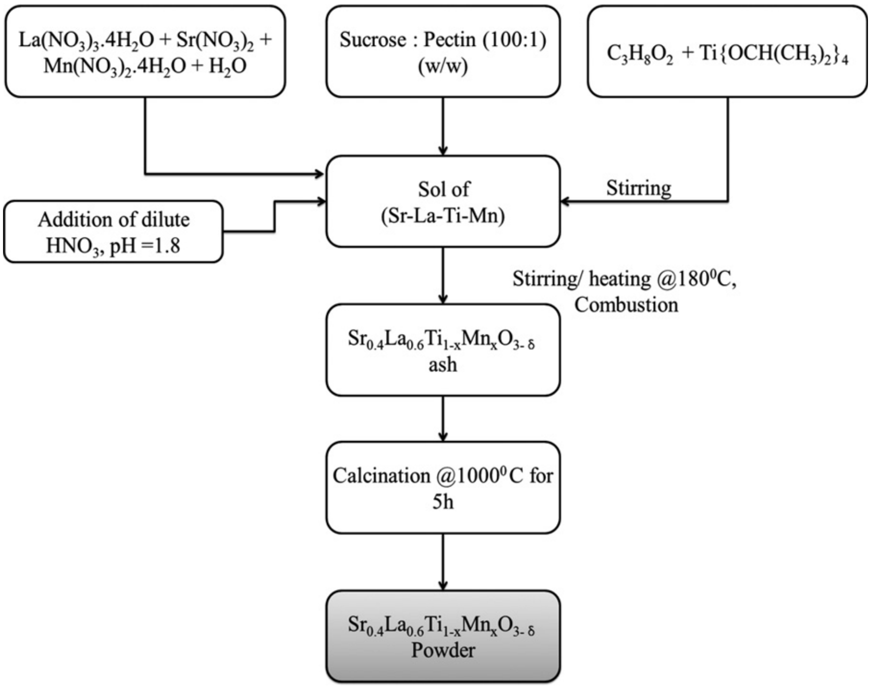

Fig. 1. Flow chart for the synthesis of the $Sr_{0.4}La_{0.6}Ti_{1-x}Mn_xO_{3-\delta}$ powders using a modified sol–gel combustion technique.

energy-dispersive X-ray spectroscopy (SEM/EDX, SN-3000 Hitachi, Japan). X-ray photoelectron spectroscopy (XPS) analysis was carried out by AXIS-NOVA (Kratos Inc.) using Al K_α (1486.6 eV) monochromatic X-ray sources at 120 W.

Thermogravimetric analysis (TGA) was performed to evaluate the carbon deposition behavior of the powders. First, $Sr_{0.4}La_{0.6}Ti_{1-x}Mn_xO_{3-\delta}$ powders were placed in a clean alumina crucible and heated at 750 °C for 6 h under flowing CH_4 at a rate of 100 $cm^3\,min^{-1}$. Then, the powders were analyzed by TGA (TA Q600, TA instruments, USA) in air in the temperature range of 30 °C to 1000 °C at a heating rate of 2 $°C\,min^{-1}$. Weight change graphs were then analyzed.

The thermal expansion coefficients (TECs) of the sintered samples were measured by thermo-mechanical analysis (TMA Q400, TA instruments, USA) from room temperature to 900 °C at a heating rate of 10 $°C\,min^{-1}$ in H_2. Electrical conductivity was measured by means of a four-probe DC method in the temperature range of 100–800 °C in H_2. Samples for the TEC and electrical conductivity measurements were sintered at 1400 °C for 4 h in air.

2.3. *Electrochemical performance tests*

Electrochemical performance tests were carried out with electrolyte supported-type single cells. Commercial GDC powder (CGO90/10 UHSA, Grand C&M Co. Ltd.) was compressed by cold iso-static pressing (CIP) and was then fired at 1450 °C for 4 h to fabricate a 0.5-mm-thick GDC electrolyte pellet. A $Sr_{0.4}La_{0.6}Ti_{1-x}Mn_xO_{3-\delta}$ anode layer was screen-printed onto the GDC pellets and was then fired at 1250 °C for 5 h. Similarly, the BSCF–GDC cathode layer was screen-printed onto the other side of the GDC pellets in a symmetric position followed by firing at 1050 °C for 2 h. The geometrical area of both electrodes was 0.49 cm^2. A seal between the single cell and the alumina tube was achieved with a Pyrex® glass ring. Humidified H_2 (~3% H_2O at 30 °C) and air were supplied as fuel and oxidant, respectively, at a rate of 100 $cm^3\,min^{-1}$. Humidified CH_4 was also used as a fuel to verify hydrocarbon fuel use.

AC impedance analysis was performed using a universal potentiostat with a frequency response analyzer (Bio-logic science instrument) with a three-electrode configuration under humidified H_2 and CH_4 at 800 °C. The applied frequency was in the range of 0.1 mHz to 1 MHz with a voltage amplitude of 10 mV. Current–voltage (*I*–*V*) measurements of the single cells were also performed using the three-electrode configuration.

3. Results and discussion

3.1. *Crystal structure and chemical compatibility*

The XRD patterns of the as-synthesized $Sr_{0.4}La_{0.6}Ti_{1-x}Mn_xO_{3-\delta}$ powders calcined at 1000 °C in air are shown in Fig. 2. All patterns showed a typical perovskite structure without any impurities and were matched with the rhombohedral unit cell similar to $La_{0.67}Sr_{0.33}MnO_3$ with space group *R* QUOTE *c* (JCPDS# 50-0308). The Goldschmidt tolerance factor, *t*, can be used as a measure of the deviation of the ABO_3 perovskite structure from the ideal cubic symmetry:

$$t = \frac{r_{(La,Sr)} + r_O}{\sqrt{2}(r_{(Mn,Ti)} + r_O)} \qquad (1)$$

where *r* indicates the radii of ions. Based on the ionic radii of Ti^{4+} (0.605 Å), Ti^{3+} (0.670 Å), Mn^{4+} (0.530 Å), and Mn^{3+} (0.645 Å), the calculated tolerance factor changes from 0.938 to 0.961 and increases with increasing Mn content. Similar variation is also found for the Ti-substituted $La_{0.7}Sr_{0.3}MnO_3$ [13].

The chemical stability of $Sr_{0.4}La_{0.6}Ti_{1-x}Mn_xO_{3-\delta}$ anodes with electrolyte materials such as YSZ, GDC was investigated. A physical mixture of $Sr_{0.4}La_{0.6}Ti_{0.2}Mn_{0.8}O_{3-\delta}$ with an electrolyte powder (1:1 wt/wt) was fired at 1250 °C for 10 h in air. The XRD profiles of the mixture powders after the compatibility testing are shown in Fig. 3. It is clearly seen that the GDC electrolyte is completely inert with respect to the $Sr_{0.4}La_{0.6}Ti_{0.2}$

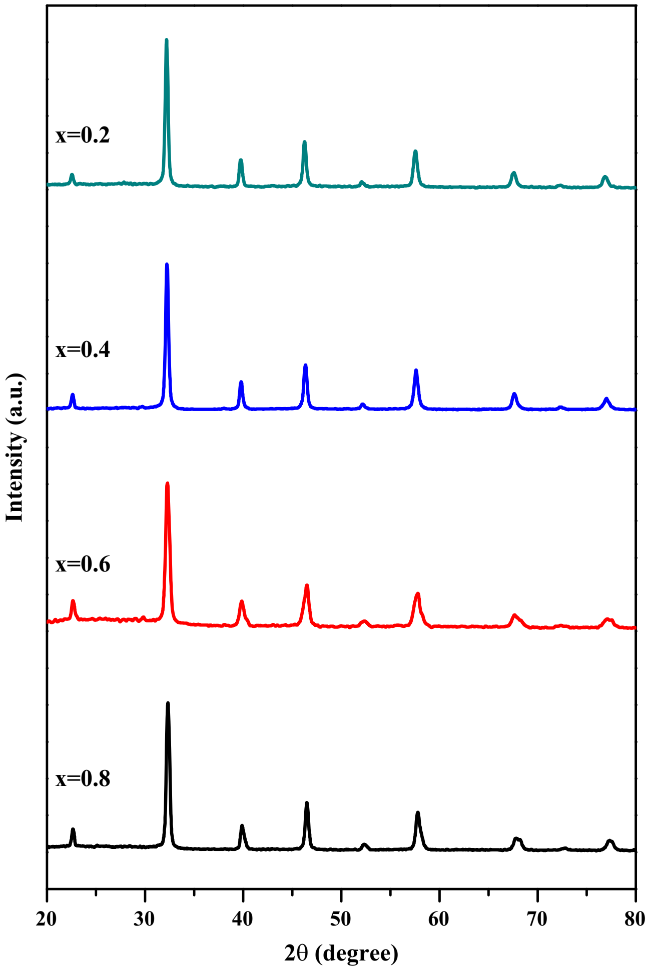

Fig. 2. XRD patterns of the $Sr_{0.4}La_{0.6}Ti_{1-x}Mn_xO_{3-\delta}$ powders calcined at 1000 °C.

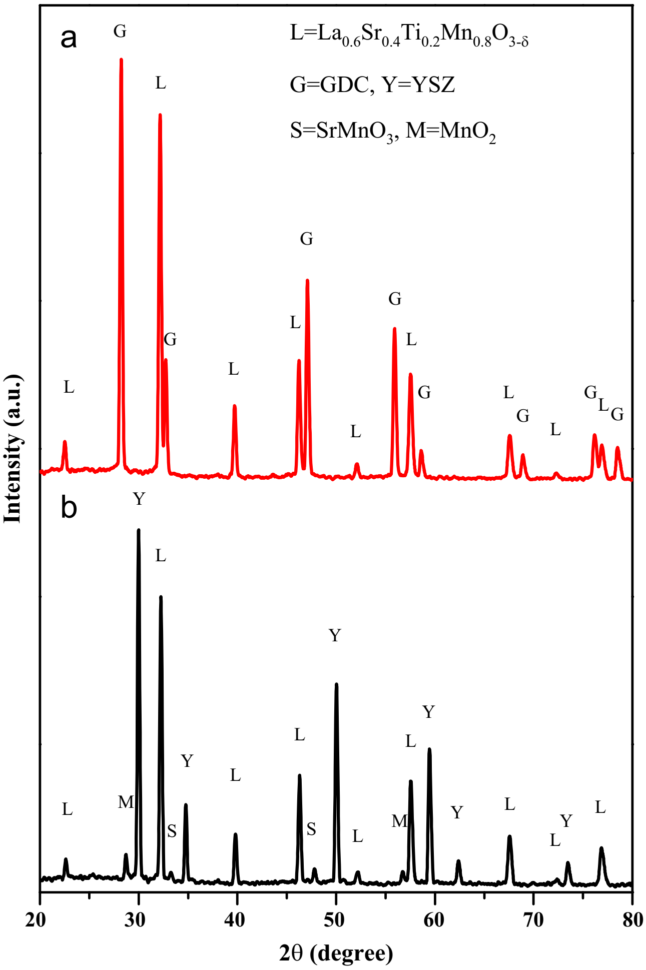

Fig. 3. XRD patterns of the physical mixtures of $Sr_{0.4}La_{0.6}Ti_{0.2}Mn_{0.8}O_{3-\delta}$ with (a) GDC and (b) YSZ after firing at 1250 °C for 10 h in air.

$Mn_{0.8}O_{3-\delta}$ anode. However, secondary phases were found in the mixture of YSZ and $Sr_{0.4}La_{0.6}Ti_{0.2}Mn_{0.8}O_{3-\delta}$. The secondary phases were indexed with MnO_2 (JCPDF# 24-0735) and $SrMnO_3$ (JCPDF# 23-1413). The formation of the MnO_2 may be due to the presence of Mn^{4+} in the $Sr_{0.4}La_{0.6}Ti_{0.2}Mn_{0.8}O_{3-\delta}$. It is generally known that Mn^{4+} is aggressively soluble in cubic YSZ [4,12].

3.2. Defect structure by XPS analysis

The wide spectra of the XPS analysis for $Sr_{0.4}La_{0.6}Ti_{1-x}Mn_xO_{3-\delta}$ are shown in Fig. 4, which reveal the existence of La, Sr, Mn, Ti, O, and C signals only. The carbon signal observed may be generated by atmospheric carbon when the sample surface was exposed to air. The peaks of Ti 3p (32 eV), Mn 3s (88 eV), La 4d (106 eV), Sr 3d (130 ± 1 eV), Sr 3p (269 eV), C 1s (285 eV), Ti 2p (457 eV), O 1s (529 eV), Ti 2s (561 eV), Mn 2p (640 ± 1 eV), La 3d (835 ± 1 eV), O KLL (975 ± 1 eV), and Ti LMM (1106 eV, 1130 eV and 1175 eV) can be matched from the data available from the *NIST X-ray Photoelectron Spectroscopy Database*. The oxidation state of Sr and La in the A-sites is clearly detected as 2+ and 3+, respectively. Since the oxidation state and ratio of the B-site transition metal play a critical role in the transport properties and electrochemical performance, the XPS analysis of $Ti^{3+/4+}$ and $Mn^{3+/4+}$ will be presented in detail.

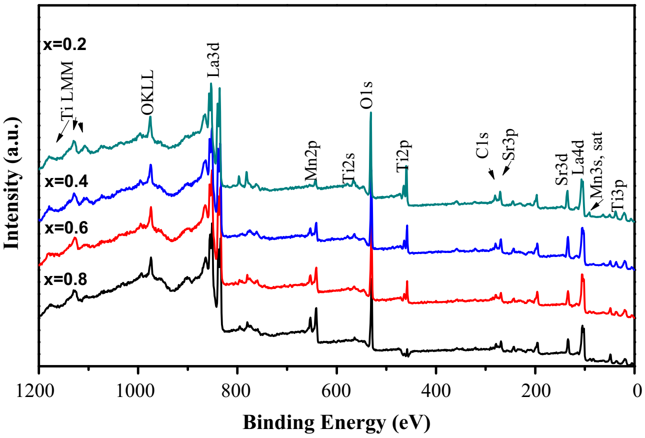

Fig. 4. XPS spectra of the $Sr_{0.4}La_{0.6}Ti_{1-x}Mn_xO_{3-\delta}$ anode materials.

3.2.1. Mn 2p spectra

The XPS spectra of Mn $2p_{1/2}$ and Mn $2p_{3/2}$ core-levels of $Sr_{0.4}$ $La_{0.6}Ti_{1-x}Mn_xO_{3-\delta}$ are shown in Fig. 5. The full width at half maximum (FWHM) of the Mn $2p_{3/2}$ peaks for all the samples was larger than 3 eV, which explicitly indicates the coexistence of Mn^{3+} and Mn^{4+} ions. From the deconvolution of the Mn 2p peak profiles, the Mn 2p peaks can be split into five distinct peaks, which are Mn^{3+} (Mn $2p_{3/2}$), Mn^{3+} (Mn $2p_{1/2}$), Mn^{4+} (Mn $2p_{3/2}$), Mn^{4+} (Mn $2p_{3/2}$), and satellite peaks of Mn, corresponding to 640.8 eV and 653.4 eV, 642.2 eV, 652.5 eV, and 646.4 eV, respectively [14–21]. The exact peak positions and the ratio of Mn^{3+}/Mn^{4+} calculated from peak areas are listed in Table 1. As shown, the ratio of Mn^{3+}/Mn^{4+} increases with an increase in the Mn content. This indicates that charge compensation can occur by the reduction of Mn^{4+} to Mn^{3+} as well as the reduction of Ti, and the amount of Mn^{3+} increases with increasing Mn content.

3.2.2. Ti 2p spectra

The XPS spectra of Ti 2p for $Sr_{0.4}La_{0.6}Ti_{1-x}Mn_xO_{3-\delta}$ are shown in Fig. 6. Ti 2p peaks can split into Ti $2p_{3/2}$ and Ti $2p_{1/2}$ due to spin–orbital splitting. Deconvoluting the Ti 2p peak results in three distinct peaks of Ti^{4+} (Ti $2p_{3/2}$), Ti^{3+} (Ti $2p_{1/2}$), and Ti^{4+} (Ti $2p_{1/2}$) at 457.8 eV, 462.1 eV, and 464.3 eV, respectively [21–27]. The exact peak positions and the ratio of Ti^{3+}/Ti^{4+} calculated from peak areas are listed in Table 2. Similar to the variation in the Mn^{3+}/Mn^{4+} ratio, the ratio of Ti^{3+}/Ti^{4+} increases with an increase in the Mn content. Interestingly, the Ti^{3+}/Ti^{4+} ratio is much greater than the Mn^{3+}/Mn^{4+} ratio

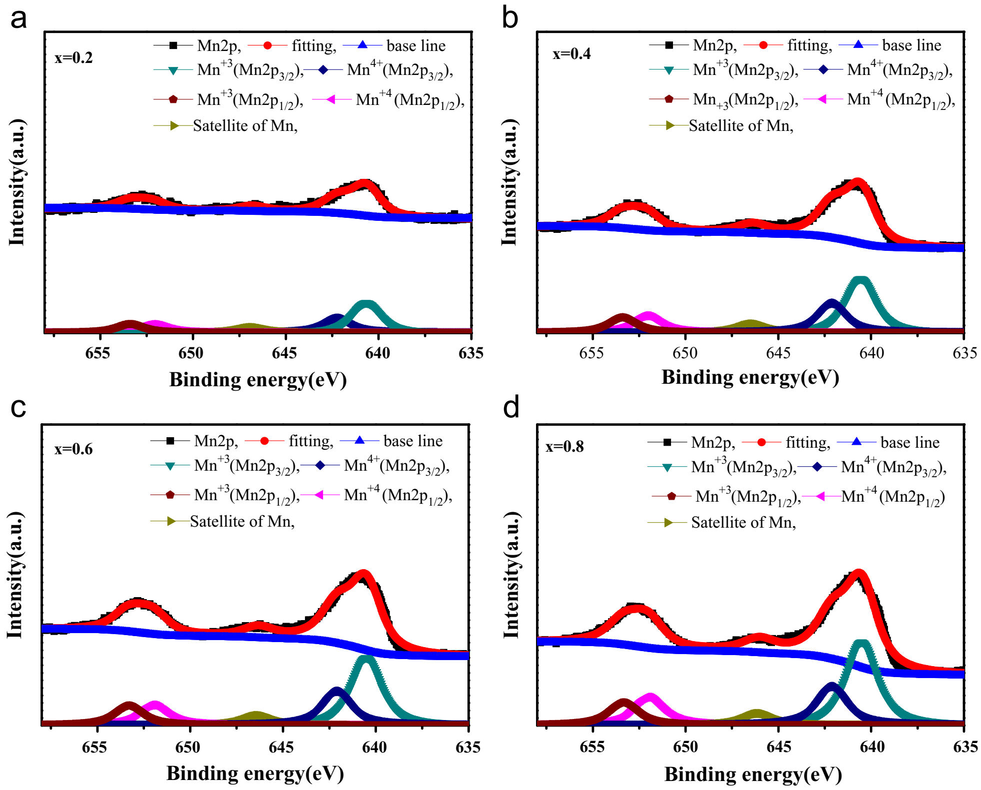

Fig. 5. XPS spectra of Mn $2p_{3/2}$ and Mn $2p_{1/2}$ of the $Sr_{0.4}La_{0.6}Ti_{1-x}Mn_xO_{3-\delta}$ anode materials.

Table 1
The binding energy for Mn $2p_{3/2}$ and Mn $2p_{1/2}$ of the $Sr_{0.4}La_{0.6}Ti_{1-x}Mn_xO_{3-\delta}$ anodes by deconvoluting Mn 2p spectra.

Composition	Peak position (eV)					Mn^{3+}/Mn^{4+}
	Mn^{3+} (Mn $2p_{3/2}$)	Mn^{4+} (Mn $2p_{3/2}$)	Satellite of Mn	Mn^{4+} (Mn $2p_{1/2}$)	Mn^{3+} (Mn $2p_{1/2}$)	
$x=0.2$	640.64	642.25	646.80	652.16	653.48	1.65
$x=0.4$	640.56	642.11	646.37	652.13	653.39	1.81
$x=0.6$	640.51	642.09	646.32	652.01	653.28	1.96
$x=0.8$	640.50	641.92	646.03	651.98	653.26	2.12

(Table 1). This indicates that the charge compensation in $Sr_{0.4}La_{0.6}Ti_{1-x}Mn_xO_{3-\delta}$ occurs dominantly by the reduction of Ti^{4+} to Ti^{3+} compared to the Mn reduction.

3.3. Thermal expansion behavior

The thermal expansion curves of the $Sr_{0.4}La_{0.6}Ti_{1-x}Mn_xO_{3-\delta}$ anodes in H_2 are given in Fig. 7. The calculated average linear thermal expansion coefficient (TEC) values of the $Sr_{0.4}La_{0.6}Ti_{1-x}Mn_xO_{3-\delta}$ anodes in H_2 were 11.3×10^{-6} K^{-1}, 10.4×10^{-6} K^{-1}, 10.2×10^{-6} K^{-1}, and 9.46×10^{-6} K^{-1} for $x=0.2$, 0.4, 0.6, and 0.8, respectively, which is comparable with that of GDC electrolyte (12.5×10^{-6} K^{-1}) [28]. A similar TEC value of 10.8–14.5×10^{-6} K^{-1} has been observed in the analogous $(La_{0.75-x}Sr_{0.25+x})_{0.95}Mn_{0.5}Cr_{0.5-x}Ti_xO_{3-\delta}$ ($x=0$–0.5) [29]. The calculated TEC value of $Sr_{0.4}La_{0.6}Ti_{1-x}Mn_xO_{3-\delta}$ decreased with increasing Mn content. TEC is inversely proportional to bonding energy between ions in the lattice [30,31]. Khowash and Ellis reported that the Mn–O bond is stronger than the Ti–O bond [32]. Thus, the increase in bonding energy with Mn doping could also cause a decrease in TEC.

3.4. Thermo-gravimetric analysis

Thermo-gravimetric analysis for the $Sr_{0.4}La_{0.6}Ti_{1-x}Mn_xO_{3-\delta}$ powders exposed to CH_4 at 750 °C for 6 h were carried out in air to investigate the oxygen storage capability and the carbon deposition rate. The weight change vs. temperature curves are shown in Fig. 8. During the reduction process of the $Sr_{0.4}La_{0.6}Ti_{1-x}Mn_xO_{3-\delta}$

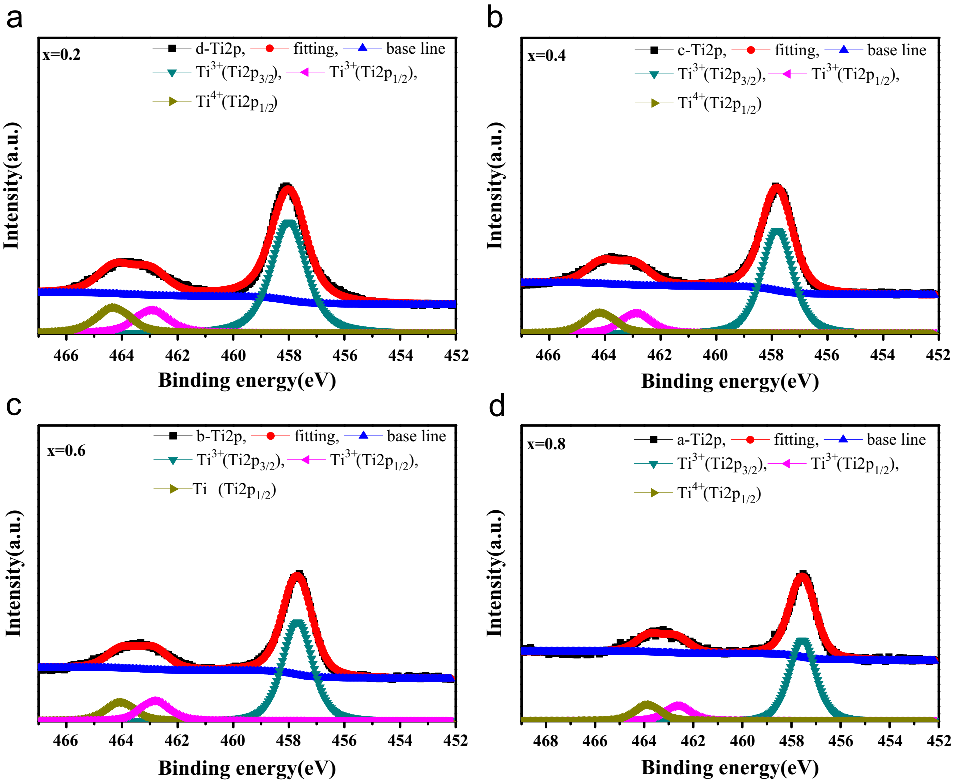

Fig. 6. XPS spectra of Ti $2p_{3/2}$ and Ti $2p_{1/2}$ of the $Sr_{0.4}La_{0.6}Ti_{1-x}Mn_xO_{3-\delta}$ anode materials.

Table 2
The binding energy for Ti $2p_{3/2}$ and Ti $2p_{1/2}$ of the $Sr_{0.4}La_{0.6}Ti_{1-x}Mn_xO_{3-\delta}$ anodes by deconvoluting Ti 2p spectra.

Composition	Peak position (eV)			Ti^{3+}/Ti^{4+}
	Ti^{3+} (Ti $2p_{3/2}$)	Ti^{3+} (Ti $2p_{1/2}$)	Ti^{4+} (Ti $2p_{1/2}$)	
$x=0.2$	454.0	463.0	464.25	5.27
$x=0.4$	457.82	462.92	464.11	5.93
$x=0.6$	457.70	462.90	464.04	6.31
$x=0.8$	457.54	462.7	463.7	7.09

powders at 750 °C in CH_4 for 6 h, the lattice oxygen can be removed to form oxygen vacancies, and cracked carbon from CH_4 is deposited onto the sample surface.

According to the weight gain or loss behavior in the TGA plot, four distinct regions can be identified: Region I ($\sim 400 \pm 5$ °C), Region II (400 ± 5–500 ± 2 °C), Region III (500 ± 2–800 ± 5 °C), and Region IV (800 ± 5 °C$\sim$). Weight gain in Region I occurs due to the α-oxygen adsorption, which is a superficial process or is frozen-in, and weight loss in Region II indicates the oxidation of the deposited carbon. The second weight gain (Region III) and loss (Region IV) can be matched with the β-oxygen absorption/incorporation at high temperature and the oxygen release accompanied by the thermal reduction of $Mn^{3+} \rightarrow Mn^{2+}$, respectively. Meanwhile, the re-oxidation process, which accumulates some oxygen into the reduced $Sr_{0.4}La_{0.6}Ti_{1-x}Mn_xO_{3-\delta}$, can be characterized in terms of the oxygen storage capability (OSC), which is the sum of the α-oxygen adsorption and the β-oxygen absorption/incorporation at high temperature [33]. Quantitative analysis data for TGA are listed in Table 3.

Since Ti^{4+} is more stable than Mn^{4+} at high temperature, the formation of oxygen vacancies might be controlled by the reduction of Mn^{4+} to Mn^{3+}, and the amount of oxygen vacancies in the reduced samples consequently increase with the Mn content. In addition, the amount of oxygen adsorption and incorporation is proportional to the amount of oxygen vacancies on the surface. Therefore, weight gain in Regions I and III increase with increasing Mn content. Tao and Irvine reported a similar weight gain behavior for $(La_{0.75}Sr_{0.25})Cr_{0.5}Mn_{0.5}O_{3-\delta}$ anode materials [2]. The weight loss corresponding to the oxidation of the deposited carbons decreases with increasing Mn content. During the reduction of $Sr_{0.4}La_{0.6}Ti_{1-x}Mn_xO_{3-\delta}$ in CH_4, the released oxygen can oxidize the carbon deposits. In this regard, the Mn-rich compositions, which have large

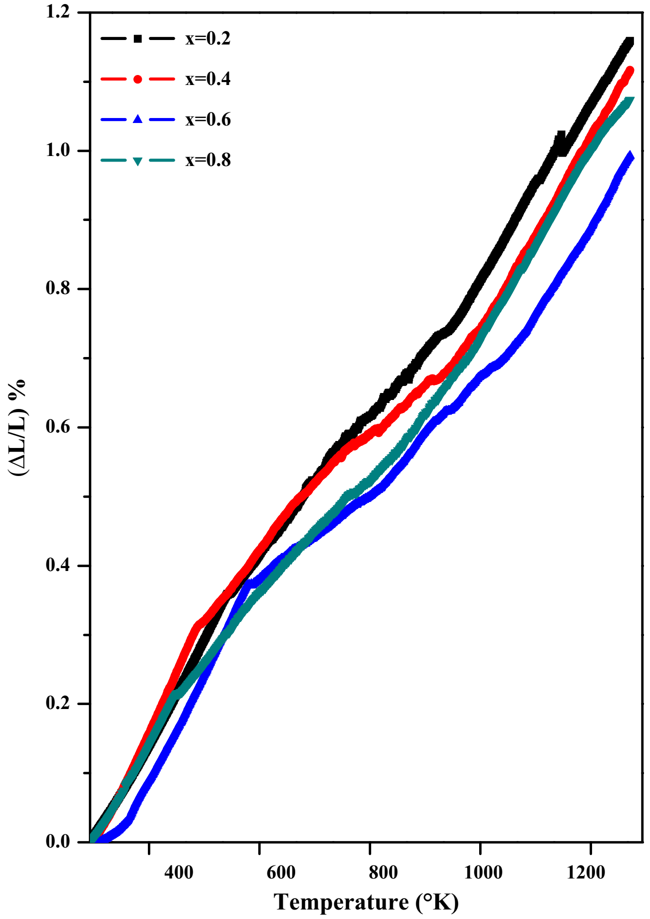

Fig. 7. Thermal expansion curves as a function of temperature for the $Sr_{0.4}La_{0.6}Ti_{1-x}Mn_xO_{3-\delta}$ anodes in H_2.

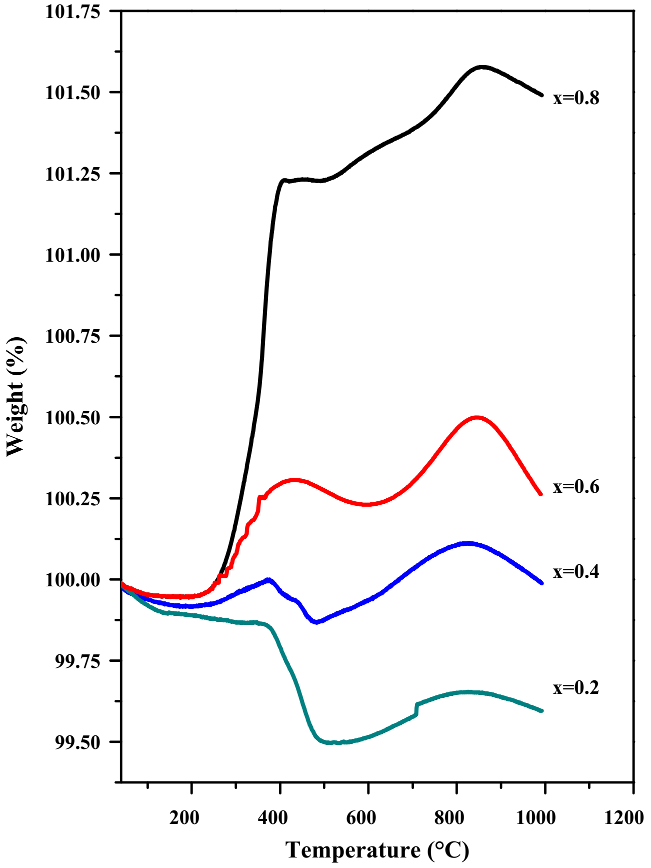

Fig. 8. TGA plots of the $Sr_{0.4}La_{0.6}Ti_{1-x}Mn_xO_{3-\delta}$ anodes recorded in air at a heating rate of 2 °C·min^{-1}.

amounts of oxygen vacancies generated by the reduction process, have a lower carbon deposition rate than the Ti-rich compositions.

3.5. Electrical conductivity

Electrical conductivities of $Sr_{0.4}La_{0.6}Ti_{1-x}Mn_xO_{3-\delta}$ measured in a H_2 atmosphere are shown in Fig. 9. At a given temperature, the electrical conductivity increased with an increase in Mn content. It is well known that La-doped $SrTiO_3$ shows n-type semi-conduction in a reducing atmosphere. Therefore, the electrical conductivity of $Sr_{0.4}La_{0.6}Ti_{1-x}Mn_xO_{3-\delta}$ is essentially controlled by the concentration of charge carrier such as an electronic defect (Ti^{3+}, $[Ti'_{Ti}]$ and/or Mn^{3+}, $[Mn'_{Mn}]$). As shown in the XPS analysis, the amounts of Mn^{3+} and Ti^{3+} increase with the Mn content, resulting in an increase in electrical conductivity at a given temperature. Moreover, the formation of oxygen vacancies in the reduced atmosphere can accompany the reduction of Mn^{4+} to Mn^{3+} and Ti^{4+} to Ti^{3+}, which leads to an increased amount of charge carriers. The TGA data in Fig. 8 also show that the amount of oxygen vacancies increases with increasing Mn content, which implies increased concentrations of Mn^{3+} and Ti^{3+}.

The calculated activation energies of the $Sr_{0.4}La_{0.6}Ti_{1-x}Mn_xO_{3-\delta}$ anodes were 0.809 eV, 0.510 eV, 0.501 eV, and 0.500 eV for $x=0.2$, 0.4, 0.6, and 0.8, respectively. The activation energy (E_a) for the hopping of a small polaron such as an electron is given as [34]:

$$E_a = \frac{E_p}{2} - W \tag{2}$$

where E_p and W are the polaron binding energy and bandwidth, respectively. The decrease in the activation energy with x in the $Sr_{0.4}La_{0.6}Ti_{1-x}Mn_xO_{3-\delta}$ anodes implies a reduction in the polaron binding energy or an increase in the bandwidth. This behavior could be understood by considering the changes in the structural parameters with Mn doping. As discussed in the crystal structure, the Goldschmidt tolerance factor indicating the crystal symmetry changes from 0.938 to 0.961 for the $Sr_{0.4}La_{0.6}Ti_{1-x}Mn_xO_{3-\delta}$ anodes and increases with increasing Mn content. Both the bandwidth and the magnetic exchange interaction are closely related to the deviation of the bond angle from the ideal value of 180° [35]. Mn doping leads to an increase in the tolerance factor and the O–(Ti,Mn)–O bond angle toward 180°, resulting in an increase in the overlap between the Mn-3d

Table 3
Quantitative analysis data based on the TGA experiment for the $Sr_{0.4}La_{0.6}Ti_{1-x}Mn_xO_{3-\delta}$ anodes exposed to CH_4 at 750 °C for 6 h.

Composition	α-oxygen adsorption (μmol g^{-1})	Carbon deposition (μmol g^{-1})	β-oxygen absorption (μmol g^{-1})	OSC (μmol g^{-1} of O_2)
$x=0.2$	–	255.5	56.5	56.5
$x=0.4$	50.7	106.6	77.2	127.9
$x=0.6$	304.8	86.2	97.7	402.5
$x=0.8$	798.8	10.0	114.6	913.4

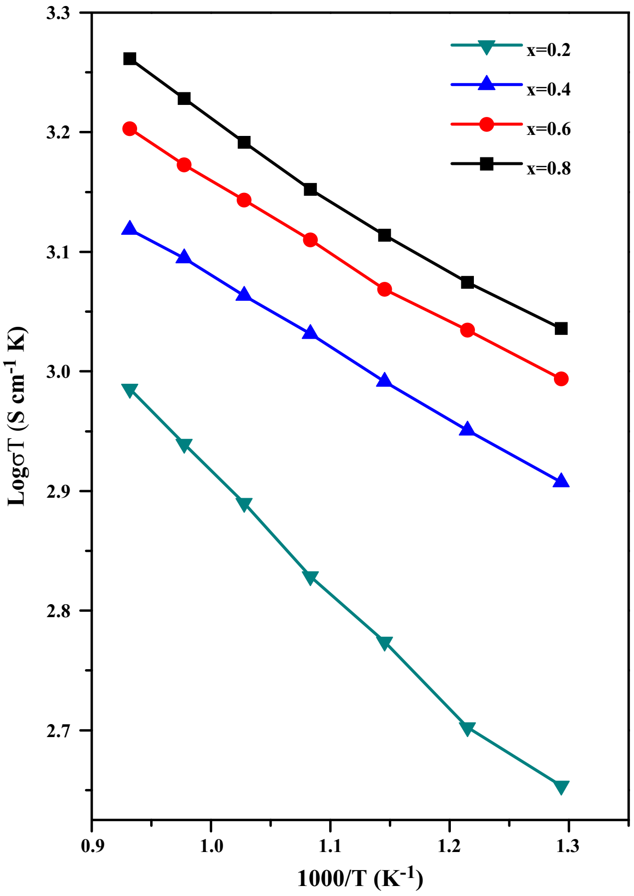

Fig. 9. Variation of electrical conductivities of $Sr_{0.4}La_{0.6}Ti_{1-x}Mn_xO_{3-\delta}$ anodes in humidified H_2 (97% H_2+3% H_2O).

(or Ti-3d) and O-2p orbitals and the bandwidth. Similar results have been reported for the Co-based perovskite oxide systems [36]. Additionally, the straightening of the O–(Ti,Mn)–O bonds can relieve the deep localization of charge carriers and thereby decreases E_p. Thus, the increase in bandwidth and the decrease in polaron binding energy lead to a decrease in the activation energy with increasing Mn content.

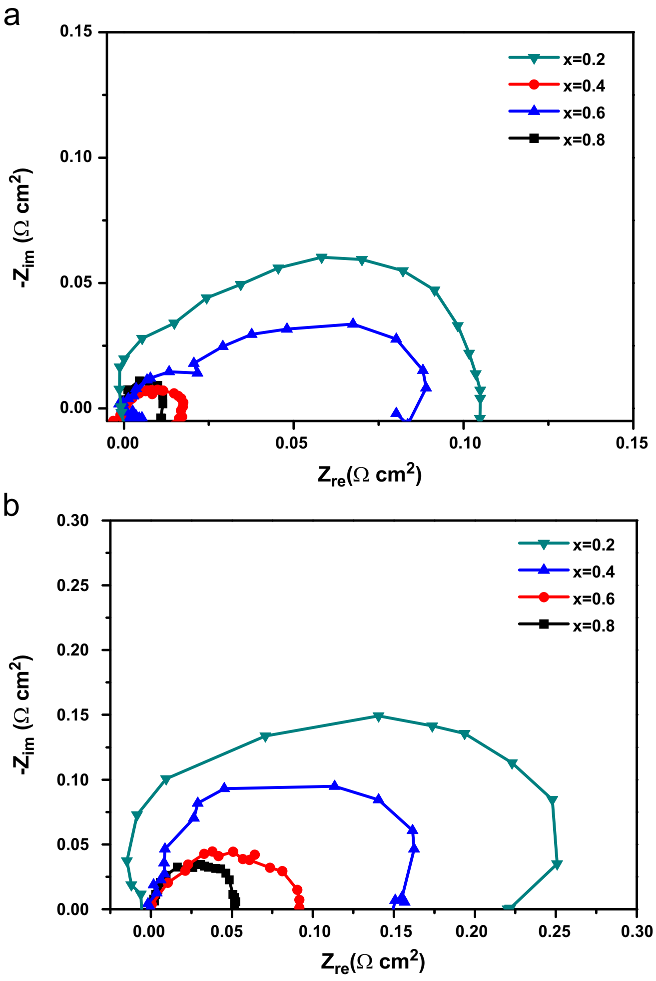

Fig. 10. Typical AC impedance spectra of the $Sr_{0.4}La_{0.6}Ti_{1-x}Mn_xO_{3-\delta}$ anodes in humidified (a) H_2 and (b) CH_4 atmospheres at 800 °C.

3.6. Electrochemical performance

Electrochemical performances of the $Sr_{0.4}La_{0.6}Ti_{1-x}Mn_xO_{3-\delta}$ anodes were evaluated by AC-impedance spectroscopy and *I–V* measurement with electrolyte supported-type single cells. The AC impedance spectra of the $Sr_{0.4}La_{0.6}Ti_{1-x}Mn_xO_{3-\delta}$ anodes in both H_2 and CH_4 at 800 °C are shown in Fig. 10, and the calculated anode polarization resistance, R_p, values are provided in Table 4. The magnitude of the R_p value in CH_4 is much larger than that in H_2 due to surface reactions on the anode. Considering the oxidation of H_2 via the CH_4 reforming process and slow pore diffusion of CH_4 molecules with larger size compared to H_2 molecules, the single cell operated in H_2 should show better performance than the single cell operated in CH_4. The R_p value of the $Sr_{0.4}La_{0.6}Ti_{1-x}Mn_xO_{3-\delta}$ anodes in H_2 decreased with increasing dopant content. This is due to a doping-induced increase in both electrical conductivity and catalytic activity. In general, the anode reaction in SOFCs is considered a multiphase catalytic reaction. Therefore, hydrogen reduction at a porous anode is limited not only by the charge transfer and the adsorption/dissociation of hydrogen on anode surface, but also by the transport of oxide ions through the anode bulk and across the anode/electrolyte interface. In this regard, anode polarization is closely related to the kinetics of surface exchange and diffusion in anode materials as well as the electronic conductivity. Both the concentration of oxygen vacancies and electrical conductivity increased with increasing Mn doping, as is evident from the data in Fig. 8 and Fig. 9. Thus, the increasing oxygen vacancy concentration and electrical conductivity with Mn doping appear to increase the surface exchange and the transport speed of oxide ions as well as the charge transfer, leading to an increase in the electrochemical performance. Meanwhile, the R_p values in CH_4 also increased with increasing Mn content. The limitation to gas diffusion in CH_4 could be caused by carbon deposits, which may subsequently block the anode pores. Moreover, the carbon deposits may cover the reaction sites, leading to a decrease in catalytic activity. The variation in R_p values in CH_4 showed the same trends as observed for the carbon deposition rate, as shown in Fig. 8 and Table 3. Consequently, Mn doping could reduce the carbon deposition rate, resulting in improved electrochemical performance in CH_4 fuel.

Table 4
Polarization resistance of the $Sr_{0.4}La_{0.6}Ti_{1-x}Mn_xO_{3-\delta}$ anodes at 800 °C in humidified H_2 and CH_4 fuels.

Composition	Polarization resistance (Ω cm^2)	
	In H_2	In CH_4
$x=0.2$	0.107	0.219
$x=0.4$	0.089	0.149
$x=0.6$	0.017	0.091
$x=0.8$	0.011	0.054

The variation of the power densities with current density at 800 °C for the various $Sr_{0.4}La_{0.6}Ti_{1-x}Mn_xO_{3-\delta}$ anode compositions are shown in Fig. 11. The open circuit voltages at 800 °C were 0.7 ± 0.05 V due to the reduction of GDC electrolyte in a reducing atmosphere. The power densities in both H_2 and CH_4 increase with increasing Mn content, which shows the same trends as observed for the AC-impedance spectroscopy analysis in Fig. 10. The maximum power densities of the single cell with the $Sr_{0.4}La_{0.6}Ti_{0.2}Mn_{0.8}O_{3-\delta}$ anode in H_2 and CH_4 were 0.29 W cm^{-2} and 0.24 W cm^{-2}, respectively. Interestingly, all the compositions showed excellent recovery performance, which was measured after re-oxidation in a H_2 atmosphere. The recovery rate for all the $Sr_{0.4}La_{0.6}Ti_{1-x}Mn_xO_{3-\delta}$ anode materials was greater than 86%, which is a much higher value than the recovery rate of 46% for the Ni–GDC anode [37].

4. Conclusions

New redox-stable $Sr_{0.4}La_{0.6}Ti_{1-x}Mn_xO_{3-\delta}$ ($x=0.2$, 0.4, 0.6, and 0.8) anode materials are successfully synthesized

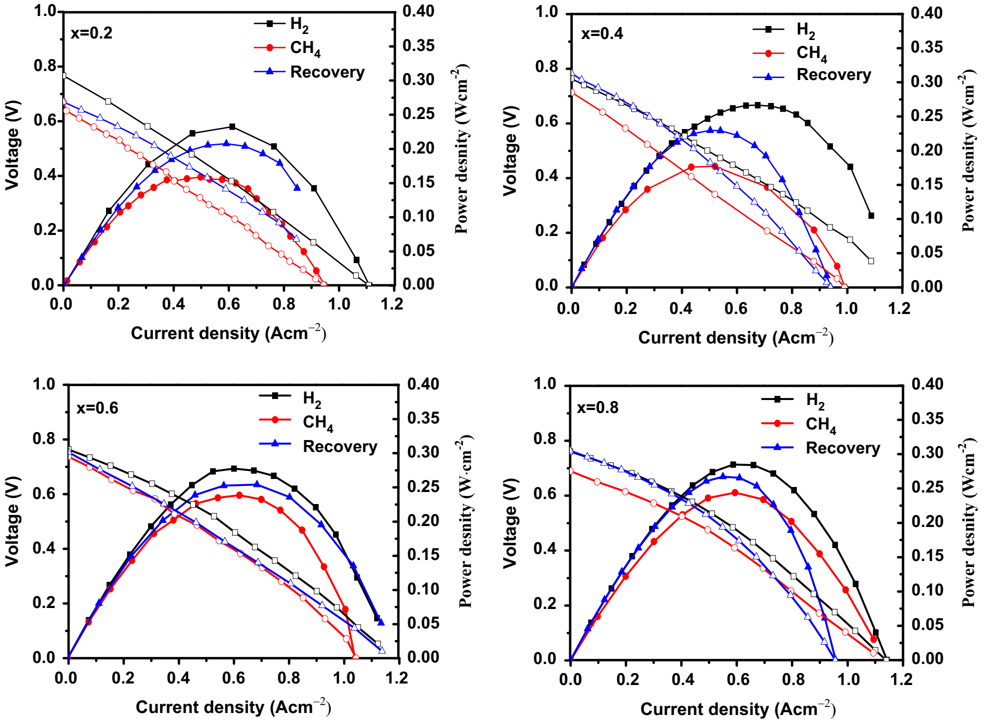

Fig. 11. Comparison of the I–V curves and power densities of the $Sr_{0.4}La_{0.6}Ti_{1-x}Mn_xO_{3-\delta}$ anodes at 800 °C.

by a simple modified sol–gel combustion route. While the partial replacement of Ti by Mn lowered the TEC, it leads to an increase in electrical conductivity due to the modification of the defect and electronic structures of the $Sr_{0.4}La_{0.6}Ti_{1-x}Mn_xO_{3-\delta}$ anodes.

Based on the X-ray photoelectron spectroscopy analysis, it is clear that the amount of Mn^{3+} and Ti^{3+} increases with Mn doping. The increase in electrical conductivity as well as oxygen vacancy concentration in a reducing atmosphere results in an increase in the catalytic activity for the H_2 oxidation reaction in SOFCs due to an increase in the surface exchange, oxide ion mobility, and charge transfer kinetics. The carbon deposition rate decreased with Mn doping, and $Sr_{0.4}La_{0.6}Ti_{1-x}Mn_xO_{3-\delta}$ materials showed much lower deposition of carbon compared with the conventional Ni–YSZ cermet anodes. It should be mentioned that the $Sr_{0.4}La_{0.6}Ti_{1-x}Mn_xO_{3-\delta}$ anodes showed high power density for CH_4 fuel with redox-stability. Therefore, $Sr_{0.4}La_{0.6}Ti_{1-x}Mn_xO_{3-\delta}$ oxides are promising candidates as anode materials for CH_4-fueled SOFCs.

Acknowledgements

This research was supported by a grant from the Fundamental R&D Program for Core Technology of Materials funded by the Ministry of Knowledge Economy, Republic of Korea. This work was also supported by the Human Resources Development of the Korea Institute of Energy Technology Evaluation and Planning (KETEP) funded by the Korea government Ministry of Knowledge Economy (Grant No. 20114030200060).

References

[1] N.Q. Minh, Ceramic fuel cells, Journal of the American Ceramic Society 76 (1993) 563–588.

[2] S.W. Tao, J.T.S. Irvine, Synthesis and characterization of $(La_{0.75}Sr_{0.25})Cr_{0.5}Mn_{0.5}O_{3-\delta}$, a redox-stable, efficient perovskite anode for SOFCs, Journal of the Electrochemical Society 151 (2004) A252–A259.

[3] Q.X. Fu, F. Tietz, D. Stöver, $La_{0.4}Sr_{0.6}Ti_{1-x}Mn_xO_{3-\delta}$ perovskites as anode materials for solid oxide fuel cells, Journal of the Electrochemical Society 153 (2006) D74–D83.

[4] G. Corre, G. Kim, M. Cassidy, J.M. Vohs, R.J. Gorte, J.T.S. Irvine, Activation and ripening of impregnated manganese containing perovskite SOFC electrodes under redox cycling, Chemistry of Materials 21 (2009) 1077–1084.

[5] J.H. Kim, D. Miller, H. Schlegl, D. McGrouther, J.T.S. Irvine, Investigation of microstructural and electrochemical properties of impregnated $(La,Sr)(Ti,Mn)O_{3\pm\delta}$ as a potential anode material in high-temperature solid oxide fuel cells, Chemistry of Materials 23 (2011) 3841–3847.

[6] A. Orera, P.R. Slater, New chemical systems for solid oxide fuel cells, Chemistry of Materials 22 (2010) 675–690.

[7] K. Uematsu, O. Sakurai, N. Mizutani, M. Kato, Electrical properties of La-doped $SrTiO_3$ (La: 0.1 at% to 2.0 at%) single crystals grown by xenon-arc image floating zone method, Journal of Materials Science 19 (1984) 3671–3679.

[8] O.A. Marina, N.L. Canfield, J.W. Stevenson, Thermal, electrical, and electrocatalytical properties of lanthanum-doped strontium titanate, Solid State Ionics 149 (2002) 21–28.

[9] R. Moos, K.H. Härdtl, Electronic transport properties of $Sr_{1-x}La_xTiO_3$ ceramics, Journal of Applied Physics 80 (1996) 393–400.

[10] D. Miller, J.T.S. Irvine, B-site doping of lanthanum strontium titanate for solid oxide fuel cell anodes, Journal of Power Sources 196 (2011) 7323–7327.

[11] S.W. Tao, J.T.S. Irvine, A redox-stable efficient anode for solid-oxide fuel cells, Nature Materials 2 (2003) 320–323.

[12] J.C. Ruiz-Morales, J. Canales-Vasquez, C. Savaniu, D. Marrero-Lopez, W. Zhou, J.T.S. Irvine, Disruption of extended defects in solid oxide fuel cell anodes for methane oxidation, Nature 439 (2006) 568–571.

[13] M.S. Kim, J.B. Yang, Q. Cai, X.D. Zhou, W.J. James, W.B. Yelon, P.E. Parris, D. Buddhikot, S.K. Malik, Structure, magnetic, and transport properties of Ti-substituted $La_{0.7}Sr_{0.3}MnO_3$, Physical Review B: Condensed Matter 71 (2005) 014433.

[14] M.C. Biesinger, B.P. Payne, A.P. Grosvenor, L.W.M. Lau, A.R. Gerson, C. Smart, Resolving surface chemical states in XPS analysis of first row transition metals, oxides and hydroxides:Cr, Mn, Fe, Co and Ni, Applied Surface Science 257 (2011) 2717–2730.

[15] X.H. Xia, L. Lu, A.S. Walton, M. Ward, X.P. Han, R. Brydson, J.K. Luo, G. Shao, Origin of significant visible-light absorption properties of Mn-doped TiO_2 thin films, Acta Materialia 60 (2012) 1974–1985.

[16] H. Nesbitt, D. Banerjee, Interpretation of XPS Mn(2p) spectra of Mn oxyhydroxides and constraints on the mechanism of MnO_2 precipitation, American Mineralogist 83 (1998) 305–315.

[17] V. Di. Castro, S. Ciampi, XPS study of the growth and reactivity of Fe/MnO thin films, Surface Science 331–333 (1995) 294–299.

[18] G.C. Allen, S.J. Harris, J.A. Jutson, J.M. Dyke, A study of a number of mixed transition metal oxide spinels using X-ray photoelectron spectroscopy, Applied Surface Science 37 (1989) 111–134.

[19] B.J. Tan, K.J. Klabunde, P.M.A. Sherwood, XPS studies of solvated metal atom dispersed (SMAD) catalysts. Evidence for layered cobalt-manganese particles on alumina and silica, Journal of the American Chemical Society 113 (1991) 855–861.

[20] K. Zhang, P. Han, L. Gu, L. Zhang, Z. Liu, Q. Kong, C. Zhang, S. Dong, Z. Zhang, J. Yao, H. Xu, G. Cui, L. Chen, Synthesis of nitrogen-doped MnO/graphene nanosheets hybrid material for lithium ion batteries, Applied Materials & Interfaces 4 (2012) 658–664.

[21] M. Fujiwara, T. Matsushita, S. Ikeda, Evaluation of Mn^3s X-ray photoelectron spectroscopy for characterization of manganese complexes, Journal of Electron Spectroscopy and Related Phenomena 74 (1995) 201–206.

[22] F. Werfel, O. Brümmer, Corundum structure oxides studied by XPS, Physica Scripta 28 (1983) 92–96.

[23] V.V. Atuchin, V.G. Kesler, N.V. Pervukhina, Z. Zhang, Ti 2p and O 1s core levels and chemical bonding in titanium-bearing oxides, Journal of Electron Spectroscopy and Related Phenomena 152 (2006) 18–24.

[24] F. Guillemot, M.C. Porté, C. Labrugère, C. Baquey, Ti^{4+} to Ti^{3+} conversion of TiO_2 uppermost layer by low-temperature vacuum annealing: interest for titanium biomedical applications, Journal of Colloid and Interface Science 255 (2002) 75–78.

[25] D. Gonbeau, C. Guimon, G. Pfister-Guillouzo, A. Levasseur, G. Meunier, R. Dormoy, XPS study of thin films of titanium oxysulfides, Surface Science 254 (1991) 81–89.

[26] J.L.G. Fierro, L.A. Arrua, J.M. Lopez Nieto, G. Kremenic, Surface properties of co-precipitated V–Ti–O catalysts and their relation to the selectiveoxidation of isobutene, Applied Catalysis A: General 37 (1988) 323–338.

[27] M.C. Hsu, Y.M. Sun, I.C. Leu, M.H. Hon, Microstructural and compositional studies of liquid-phase deposition derived $PbTiO_3$ thin films on $LaNiO_3$ substrates, Applied Surface Science 253 (2007) 7639–7644.

[28] F. Tietz, H.-P. Buchkremer, D. Stöver, Components manufacturing for solid oxide fuel cells, Solid State Ionics 152–153 (2002) 373–381.

[29] V.A. Kolotygin, E.V. Tsipis, A.L. Shaula, E.N. Naumovich, J.R. Frade, S.I. Bredikhin, V.V. Kharton, Transport, thermomechanical, and electrode properties of perovskite-type $(La_{0.75-x}Sr_{0.25+x})_{0.95}Mn_{0.5}Cr_{0.5-x}Ti_xO_{3-\delta}$ (x=0–0.5), Journal of Solid State Electrochemistry 15 (2011) 313–327.

[30] H. Hayashi, M. Kanoh, C.J. Quan, H. Inaba, S. Wang, M. Dokiya, H. Tagawa, Thermal expansion of Gd-doped ceria and reduced ceria, Solid State Ionics 132 (2000) 227–233.

[31] A.R. Ruffa, Thermal expansion in insulating materials, Journal of Materials Science 15 (1980) 2258–2267.

[32] P.K. Khowash, D.E. Ellis, Electronic defect structure in TiO and MnO, Journal of Materials Science 65 (1989) 4815–4817.

[33] R.K. Hailstone, A.G. DiFrancesco, J.G. Leong, T.D. Allston, K.J. Reed, A study of lattice expansion in CeO_2 nanoparticles by transmission electron microscopy, Journal of Physical Chemistry C 113 (2009) 15155–15159.

[34] I.G. Austin, N.F. Mott, Polarons in crystalline and non-crystalline materials, Advances in Physics 18 (1969) 41–102.

[35] G.A. Sawatzky, W. Geertsma, C. Haas, Magnetic interactions and covalency effects in mainly ionic compounds, Journal of Magnetism and Magnetic Materials 3 (1976) 37–45.

[36] J.K. Burdett, Chemical Bonding in Solids, Oxford University Press, New York, 1995 167.

[37] C.K. Cho, B.H. Choi, K.T. Lee, Effect of Co alloying on the electrochemical performance of Ni–$Ce_{0.8}Gd_{0.2}O_{1.9}$ anodes for hydrocarbon-fueled solid oxide fuel cells, Journal of Alloys and Compounds 541 (2012) 433–439.